Double Higgs boson production in the 4τ channel from resonances in longitudinal vector boson scattering at a 100 TeV collider

A. V. Kotwal, S. Chekanov, and M. Low

Phys. Rev. D **91**, 114018 — Published 12 June 2015

DOI: 10.1103/PhysRevD.91.114018

Double Higgs production in the 4τ channel from resonances in longitudinal vector boson scattering at a 100 TeV collider

A. V. Kotwal
Fermi National Accelerator Laboratory, Batavia, IL 60510,
USA and Department of Physics, Duke University, Durham, NC 27708, USA

S. Chekanov
HEP Division, Argonne National Laboratory, 9700 S.Cass Avenue, Argonne, IL 60439 USA

M. Low
Department of Physics, University of Chicago, Chicago, IL 60637, USA

We discuss the sensitivity of a 100 TeV *pp* collider to heavy resonances produced in longitudinal vector boson scattering and decaying to a pair of Higgs bosons. A Monte Carlo study has been performed using the $H \to \tau\tau$ decay channel for both Higgs bosons, comparing the kinematics of such a signal to the irreducible Standard Model backgrounds. The results are presented in the context of a phenomenological model of a resonance (η) coupling to goldstone modes, $V_L V_L \to \eta \to HH$, as can arise in composite Higgs models. With a fractional width of 70% (20%), the 5σ discovery reach is 4.2 (2.9) TeV in resonance mass for 10 ab^{-1} of integrated luminosity. We also discuss the dependence of the mass reach on the collider energy and integrated luminosity.

PACS numbers: 12.38.Qk, 14.80.Rt, 12.60.Fr, 12.60.Rc, 11.10.Kk

I. INTRODUCTION

The discovery of the Higgs (H) boson [1, 2] is one of the most exciting discoveries in physics. Its discovery completes the particle spectrum predicted by the Standard Model (SM) [3, 4], and confirms the mechanism of spontaneous symmetry breaking to generate the longitudinal modes of the weak gauge bosons [5–11]. However, the issue of very large radiative corrections to the mass of fundamental scalar particles has been acknowledged for some time [12]. This is the famous "naturalness" or "fine-tuning" problem of the Higgs in the SM, where the quantum corrections due to quadratically diverging loop integrals tend to drive the parameter values towards a very high energy scale. Beyond-SM theories containing additional symmetries (such as supersymmetry or other global symmetries) are able to protect the Higgs parameters from the quadratically-divergent radiative corrections. These symmetries imply the existence of new particles in loops which cancel or mitigate the loop corrections due to SM particles.

In a class of models [13–15], the SM Higgs boson is itself another member of a set of Goldstone modes, generated from the spontaneous breaking of a larger global symmetry. Other Goldstone modes are the $W_L^\pm$ and the Z_L, which become the longitudinal components of the weak gauge bosons after electroweak symmetry breaking (EWSB). In a subset of these models [16–18], a common feature is the spontaneous breaking of a global $SO(5) \to SO(4)$ symmetry, where the four Goldstone modes are the four real components of the $SU(2)_L$ doublet Higgs field.

The spontaneous breaking of the larger global symmetry is postulated to be caused by the formation of a condensate, due to new strong dynamics at a high energy scale. As Goldstone bosons are automatically massless due to the Goldstone theorem, the question changes to why the Higgs boson mass is non-zero but small relative to the higher-energy compositeness scale. Various models have been proposed to explain this "little hierarchy" between the EWSB scale v and the new compositeness scale f_η.

A signature of this strong dynamics in the Higgs sector would be resonances coupling to the Goldstone modes, i.e. the longitudinal W and Z bosons and the Higgs boson. The lightest of such resonances would preferentially decay to the lightest particles interacting with this sector, ie. W_L, Z_L, and H. As a benchmark, we study the phenomenological model for a new scalar resonance η [19] whose Lagrangian is

$$\mathcal{L} = \mathcal{L}_{\rm SM} + \frac{1}{2}\partial^\mu\eta\partial_\mu\eta - \frac{1}{2}m_\eta^2\eta^2 + \frac{a_\eta}{f_\eta}\eta\partial^\mu\pi^a\partial_\mu\pi^a \qquad (1)$$

where π^a represents the quartet of Goldstone modes in the Higgs doublet, f_η plays the same role as the "pion decay constant" (f_π) in QCD chiral perturbation theory and a_η is a dimensionless coupling.

In composite Higgs models, rather than fully unitarizing longitudinal gauge boson scattering, the Higgs boson delays perturbative unitarity violation until the scale f_η. At this scale the strong resonances appear which together unitarize the amplitude. In the scalar resonance model we look at, there is one resonance η below the compositeness scale which partially unitarizes the amplitude, depending on the coefficient a_η. When $a_\eta = 1$ the η completely unitarizes the amplitude, hence in this work we take $a_\eta = 1$ to simplify the high-energy behavior while characterizing new strong dynamics in vector boson scattering (VBS) [20, 21]. Assuming no other decays other than to goldstones, in the high mass limit the width of the η resonance is given by [19]

$$\Gamma_\eta = \frac{a_\eta^2 m_\eta^3}{8\pi f^2} \tag{2}$$

implying that for our choice of $a_\eta = 1$ the fractional width is given by $\Gamma_\eta/m_\eta = m_\eta^2/(8\pi f^2)$.

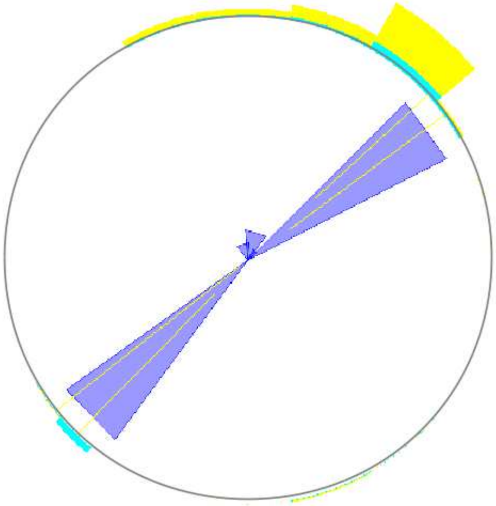

FIG. 1. A display of a simulated event generated using the process $pp \to \eta jj$ with the decay chain $\eta \to HH \to 4\tau$ at a 100 TeV pp collider, with $m_\eta = 3$ TeV. Two Higgs-jets are shown with the large blue cones, each containing a pair of τ leptons. Two small blue cones show the forward jets. The jets are reconstructed using the anti-k_T algorithm [22] using the FastJet package [23]. Yellow lines show charged hadrons.

The sensitivity to the scattering process $W_L W_L \to \eta \to W_L W_L$ at a 100 TeV pp collider has been studied [24–30]. The W^+W^- channel faces substantial background from $t\bar{t}$ production. It is interesting to probe η production using both the $V_L V_L$ and HH final states. The model predicts branching ratios in the proportions 2:1:1 for the $W_L W_L$, $Z_L Z_L$ and HH branching ratios based on counting the number of Goldstone modes in the Higgs doublet field. The distinctive feature is that Goldstone modes have purely derivative coupling, which preserves the shift symmetry of the Goldstone fields. Specifically, the coupling terms in Eqn. 1 expand to $\eta W_L^\mu W_{\mu L}$, $\eta Z_L^\mu Z_{\mu L}$, and $\eta \partial^\mu H \partial_\mu H$ respectively. The complete interaction term between the η resonance and the gauge bosons has the form $\eta[2g^2 W_\mu^+ W^{\mu -} + (g W_\mu^3 - g' B_\mu)^2]$. The specific Lorentz structure of these terms dictates the kinematic distributions associated with η production and decay. The combination of the information garnered from measuring the different branching ratios and the associated kinematic distributions can provide the definitive test of the Goldstone nature of the Higgs doublet field and information on its coupling to the new strong dynamics. Sensitivity to double-Higgs production in the context of the SM and other theoretical approaches has been investigated [31–49]. The decay channels for the Higgs boson pair are indicated in Table VI, ranked by branching ratio [50]. In this table, we require that gauge bosons decay to leptons in order to suppress enormous backgrounds from QCD jet production. The first three channels in the table, $HH \to 4b$, $HH \to 2b2\tau$, and $HH \to \ell\nu\ell\nu bb$ are subject to large QCD backgrounds from b-jets and $t\bar{t}$ production respectively. These considerations motivate the studies using the 4τ and $2\gamma 2b$ final states. The $2\gamma 2b$ final state has been studied both at 14 TeV [51–53] and 100 TeV [39, 40, 54, 55] due to its good mass resolution. In this work, we present the first study of the 4τ final state. The $2\gamma 2b$ final state may be further studied in the future as a complementary channel with different backgrounds, providing additional discovery potential.

II. THE 4τ FINAL STATE

This analysis uses all decay channels for the τ leptons from the Higgs bosons. An example of the decay $\eta \to HH \to 4\tau$ is shown in Fig. 1. It shows two Higgs bosons with transverse momenta above 1 TeV, arising from the decay of the η boson with a mass of 3 TeV. The decay of each Higgs boson leads to a single jet containing two τ leptons. The event display was created using the Delphes fast simulation [56] and the Snowmass detector setup [57]. The event, generated with the Madgraph5 Monte Carlo generator and showered with Pythia8 [58], was taken from the HepSim repository [59]. A complete color version of this event is shown in the Appendix.

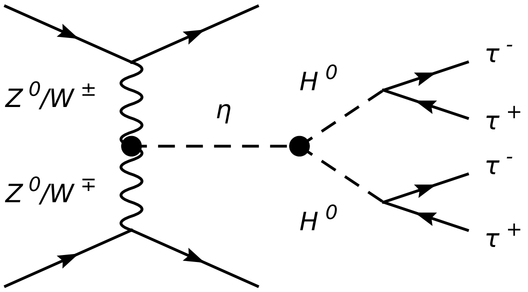

FIG. 2. Example of Feynman diagram for the process $pp \to \eta jj \to HHjj \to 4\tau + jj$ via the production of the η resonance in longitudinal vector boson fusion.

This study is performed without simulation of the detector response, but we include the effect of the τ-tagging efficiency which is the most important performance characteristic. Hence it is likely that the inclusion of a realistic detector simulation with a similar τ-tagging efficiency will not change significantly the results of this analysis. We assume that the requirement of four τ leptons will suppress mis-identification backgrounds to the level that SM processes producing four prompt τ leptons will dominate the backgrounds. This assumption is justified based on the τ-lepton identification efficiency and QCD jet rejection achieved by the LHC experiments. For instance, the hadronic decays of the τ-lepton are identified with an efficiency of 60%, and with a QCD jet efficiency of 1-2%, as reported by the ATLAS experiment [60–63]. The analysis most similar to our analysis is the high-mass $Z^{0\prime} \to \tau\tau$ search, where the transverse momenta (p_T) of the τ leptons are similar to our signal kinematics. In the double-hadronic mode, the dominant background arises from the $\gamma^*/Z \to \tau\tau$ Drell-Yan (DY) process, followed by multijet and W/Z+jet background. The latter backgrounds are a factor of 3-4 smaller than the irreducible DY background. In the leptonic+hadronic decay modes, the DY, W+jets, $t\bar{t}$, diboson and single-top backgrounds all contribute approximately equally. In order to estimate the fake backgrounds and compare them to the ZZ background for our HH search, we consider the diboson analysis for $ZV \to lljj$ [64]. This analysis shows that requiring $Z \to ll$ and $V \to jj$ with a mass window cut yields a Z+jets rate which is about 20-50 times larger than the VV rate. Given that the hadronic τ selection is about 15 times more efficient for prompt τ's compared to QCD jets, the requirement of two additional τ's will suppress the Z+jets background to a fraction of the ZZ background. Multi-jet background will be reduced to a negligible level. Reference [64] also shows that the $t\bar{t}$ background is negligible in the high $p_T(V)$ region. The requirement of two additional τ's will suppress diboson+dijet and single-top+dijet backgrounds to a negligible level.

Dedicated studies with full simulation will be needed to design the future detectors which can maintain the τ identification performance at high $p_T(\tau)$ at the same level that the LHC experiments have demonstrated. The above discussion shows that, if this performance can be achieved, the sensitivity studies presented below using the irreducible backgrounds should provide a reliable estimate of the discovery potential.

III. MONTE CARLO SIMULATIONS

The goal of this analysis is to estimate the discovery potential of a future 100 TeV scale pp collider, based on the expected event rates and distributions for the signal and backgrounds after kinematic and fiducial cuts. The τ-tagging efficiency, which is the main characteristic of detector performance, is assumed to be 60% similar to the LHC experiments [60–63].

The analysis was performed using the Pythia8 [58] and Madgraph5 [65] MC models with the default parameter settings. The MSTW2008lo68cl [66] parton density function (PDF) set was used.

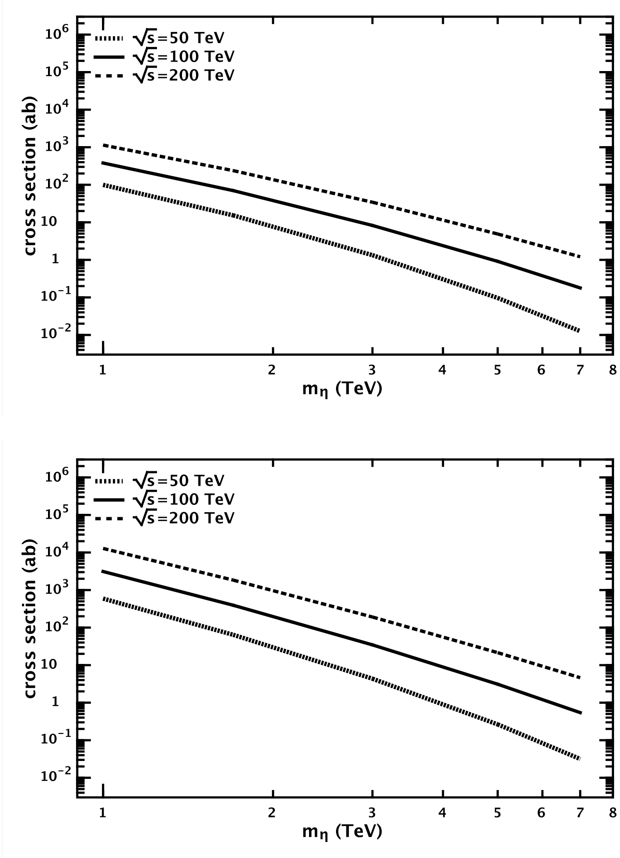

FIG. 3. Cross sections for the vector boson fusion process $pp \to \eta jj$ with $\eta \to HH \to 4\tau$ for the fractional resonance width of 20% (top) and 70% (bottom), computed using the madgraph5 program at LO QCD. The following generator-level cuts have been applied: $m_{jj} > 1.5$ TeV and $p_T(\text{jet}) > 50$ GeV.

The signal cross sections as functions of m_η are shown in Fig. 3. These cross sections scale approximately as powers of the resonance mass, m_η^{-a}, where $3.2 < a < 4.8$ ($3.9 < a < 5.2$) for a fractional resonance width of 20% (70%) and $\sqrt{s} = 100$ TeV. The range of a shows the departure from a constant-power law as $1 < m_\eta < 7$ TeV, with the larger values of a corresponding to the larger values of m_η. Thus, the value of a can be used to estimate the slope of the curves in Fig. 3 at different values of m_η. The dependence of the cross section on collider energy may also be parameterized as a power law, $(\sqrt{s})^b$, with $1.8 < b < 3.3$ ($2.2 < b < 3.6$) for a fractional resonance width of 20% (70%). Again, the range of b corresponds to $1 < m_\eta < 7$ TeV, with the larger values of b corresponding to the larger values of m_η.

The HepSim public repository [59] was used to store simulated events in the ProMC file format [67, 68]. The samples were analyzed with a C++/ROOT program [69]. The jets were reconstructed with the anti-k_T algorithm

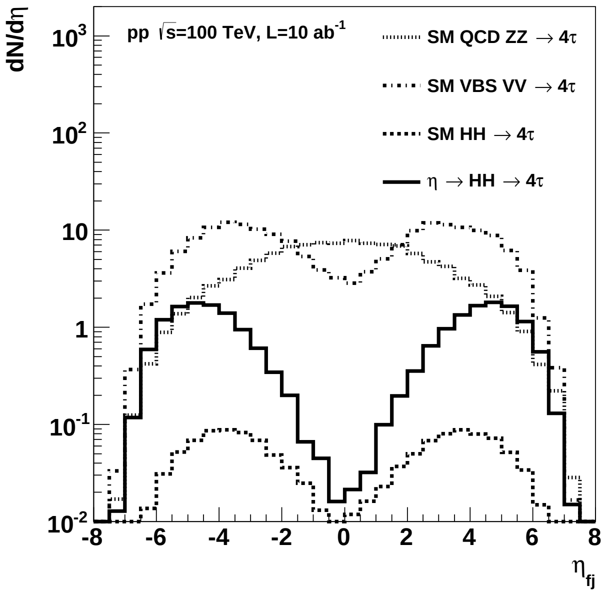

(a)The pseudo-rapidity distributions of the forward jets.

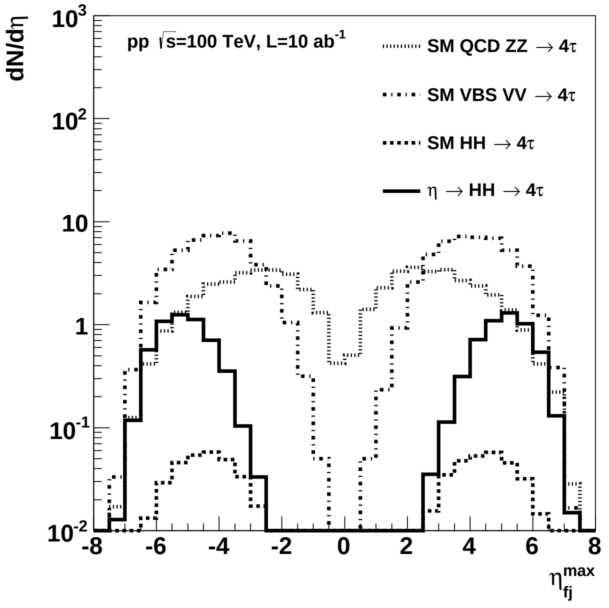

(b)The pseudo-rapidity distribution of the forward jet with larger absolute pseudo-rapidity.

FIG. 4. The pseudo-rapidity distributions of the two forward jets. Generator-level cuts $m_{jj} > 1.5$ TeV and $p_T(\text{jet}) > 50$ GeV have been applied on the jets for the samples shown. Furthermore, the generator-level cuts on the samples in all figures include $p_T(\tau) > 100$ GeV, $p_T^{\text{leading}}(\tau) > 300$ GeV and $|\eta(\tau)| < 3$. The signal distribution in all figures corresponds to $m_\eta = 3$ TeV with a fractional width of 20%.

[22] using the FastJet package [23]. The typical choice of the distance parameter R for jet reconstruction is $R \sim 0.4$ for light-quark and gluon jets, and this value is motivated for the reconstruction of the forward jets. A smaller value of $R \sim 0.05$ is motivated for the reconstruction of the highly-boosted τ-jets present in our samples. For simplicity, a single value of $R = 0.2$ is used in this study, since the kinematic distributions are fairly broad and the discrimination between signal and background is not sensitive to optimization of the choice of R. We assume that the development of sophisticated τ-reconstruction algorithms and the use of jet sub-structure information in the ultimate data analysis will permit the separation of boosted $H \to \tau\tau$ and $Z \to \tau\tau$ jets from mis-identified QCD jets and electrons mimicking τ-jets.

Jets have a generator-level requirement of $p_T(\text{jet}) > 50$ GeV, based on studies performed for the high-luminosity (HL-) LHC [70, 71] where this requirement was applied to suppress pileup jets in the forward region to an acceptable level. Given the hard dijet-mass (m_{jj}) spectrum arising from the VBS topology, a generator-level requirement of $m_{jj} > 1.5$ TeV has been applied to increase the event generation efficiency. For jet clustering, stable particles with lifetimes greater than $3 \cdot 10^{-11}$ seconds are selected, and neutrinos are excluded.

The SM background predictions were performed at leading order (LO) in QCD with the Madgraph5 program. We include the following irreducible background processes in this study; (i) $VVjj \to 4\tau jj$ production ($V = Z, \gamma^*$) via purely electroweak couplings, (ii) $ZZjj \to 4\tau jj$ production via the presence of the strong coupling in the Feynman amplitudes, and (iii) $HHjj \to 4\tau jj$ production via purely electroweak couplings. The VV production from the vector boson scattering topology was computed separately from ZZ events where the jets are radiated from QCD vertices. The interference between the $ZZjj$ amplitudes with and without QCD vertices has been shown to be about 7% in the relevant phase space at the LHC [72]. We consider this interference effect negligible for the purposes of this study. We have also neglected $HHjj$ production via gluon fusion as this contribution is suppressed by the selection requirements favoring the VBS topology. The transverse momenta of the generated τ leptons were required to be $p_T(\tau) > 100$ GeV, with the leading τ lepton required to have $p_T(\tau) > 300$ GeV, and all τ leptons are required to have pseudo-rapidity $|\eta(\tau)| < 3$, to increase the efficiency for event generation.

Next-to-leading order QCD k-factors have been estimated [73, 74] to be $\sim 50\%$ for QCD production of $VVjj$ and $< 10\%$ for VBS. As the latter background is dominant in this analysis, the relevant NLO-QCD correction is both small and similar for the signal VBS topology. Thus, NLO-QCD corrections are expected to have a negligible impact on the results.

A potential additional source of signal is the ZZ decay mode of the η resonance, via the $\eta \to ZZ \to 4\tau$ channel. Due to the factor of ~ 2 smaller branching ratio for $Z \to \tau\tau$ compared to $H \to \tau\tau$, this contribution is small compared to the signal we have considered. For simplicity we have neglected this contribution, yielding conservative results for signal sensitivity. Alternatively, the $\eta \to ZZ \to 4\tau$ channel may be distinguished from the $\eta \to HH \to 4\tau$ channel using advanced analysis techniques, and combined with the $Z \to ee/\mu\mu$ channels to check the branching ratios of the resonance to the Goldstones.

IV. KINEMATIC DISTRIBUTIONS

Figure 4 shows the pseudo-rapidity distribution of the forward jets and the distribution of pseudo-rapidity of the forward jet with larger absolute pseudo-rapidity. Forward jets are defined as the jet pair with the largest invariant mass m_{jj} in the event. Studies at the LHC have shown this criterion to be effective in identifying the forward tagging jets in VBS. The pseudo-rapidity of the more-forward jet gives an indication of the required rapidity coverage of the detector. The figures show that processes involving QCD vertices produce jets which are more central, while the VBS topology for SM and η resonance processes tends to produce jets in the forward direction. Furthermore, the η resonance process is mediated by longitudinal VBS, where the scattered quarks emerge at higher rapidities as compared to the SM VBS process mediated predominantly by transverse vector bosons. Thus, new physics that is specific to longitudinal vector bosons will be a primary driver for maximizing forward rapidity coverage.

Figure 4 motivates the requirement $|\eta(\text{jet})| > 2$ to suppress diboson production via QCD processes without significant loss of signal efficiency, hence we apply this generator-level cut for the following distributions and studies. QCD showering by PYTHIA can generate additional jets in the central region. The distribution of the difference in pseudo-rapidities $\Delta\eta_{jj}$ of the forward jets is shown in Fig. 5. This distribution motivates the additional selection requirement of $|\Delta\eta_{jj}| > 5$ after PYTHIA showering.

The scalar sum $H_T = \Sigma|\vec{p_T}|$ of all visible objects with pseudo-rapidity $|\eta| < 2.5$ in the event, called "central H_T" (H_T^c), is sensitive to QCD radiation accompanying the bosons and jets in the QCD-induced $ZZ+2j$ process. As shown in Fig. 5, the requirement $H_T^c < 300$ GeV suppresses this background.

Figure 6 shows the distribution of the p_T of the forward jets, and their m_{jj} distribution. The p_T spectrum of the forward jets emitting longitudinal vector bosons due to the signal process $V_L V_L \to \eta$ is softer than the corresponding spectra from electroweak VBS and QCD processes, motivating the cut $p_T(\text{jet}) < 500$ GeV to suppress the latter backgrounds.

The τ leptons from the $\eta \to HH \to 4\tau$ decay are produced more centrally and with higher p_T than the backgrounds. We find that good coverage of τ-jets up to $|\eta| < 3$ is adequate to have high acceptance for the signal, as shown in Fig. 7. The inclusive p_T spectrum of all τ-jets is also shown in Fig. 7. The p_T distributions of the leading and the next-to-leading τ-jets, ranked in p_T, are shown in Fig. 8.

The vector sum $\not{E}_{\mathrm{T}} = |\Sigma\vec{p_T}|$ of all detected objects, which defines the missing transverse energy, is sensitive to the angular correlations between the τ-neutrinos emitted in the decay of the τ leptons. The τ-leptons from Higgs boson decays have anti-parallel spins in the Higgs rest frame due to the Higgs being a scalar boson. Given the $V-A$ nature of the τ-lepton decay vertex, the τ neutrinos are preferentially emitted parallel to each other in the rest frame, increasing the $\not{E}_{\mathrm{T}}$. In comparison, the τ neutrinos are emitted anti-parallel to each other in Z boson rest frame due to the unit spin of the latter, preferentially reducing the $\not{E}_{\mathrm{T}}$. The distribution of $\not{E}_{\mathrm{T}}$ is shown in Fig. 9.

Additional discrimination between signal and background processes is provided by the invariant mass of combinations of τ-jets. We combine the τ-jets from a given Higgs or Z boson decay, and average the two resulting invariant masses in the event. The average reconstructed boson mass distribution is shown in Fig. 10. The peak of the reconstructed Higgs boson mass is shifted to a higher value compared to the reconstructed Z boson mass, as expected. The use of sophisticated mass-reconstruction techniques that have been developed for di-τ resonances may be used to recover information lost with the neutrinos, which may compensate for the experimental resolution on the visible momenta. Also shown in this figure are the distributions of the invariant mass all τ-jets, and the combination of all τ-jets and $\not{E}_{\mathrm{T}}$ setting the $\not{E}_{\mathrm{z}} = 0$.

V. RESULTS

After applying the selection cuts, the dominant irreducible background with the 4τ final state is $ZZ \to 4\tau$ production in the VBS topology. We combine the information in the following distributions: the p_T of the forward tagging jets and their pseudo-rapidity separation, the p_T of the leading and sub-leading τ jets, the $\not{E}_{\mathrm{T}}$, the H_T^c, the average di-τ mass, the all-τ mass and the all-τ+$\not{E}_{\mathrm{T}}$ mass, using a Boosted Decision Tree (BDT) algorithm to separate the $\eta \to HH \to 4\tau$ signal from the VBS $ZZ \to 4\tau$ background. The resulting distributions of the BDT score for the signal and this dominant background are shown in Fig. 12. We quantify the discovery reach for the signal by computing the quantity $CL_b = P(Q < Q_{obs}|b)$, the probability for the test-statistic Q to be smaller than the observed value given the background-only hypothesis. When $1 - CL_b < 2.8 \times 10^{-7}$ the background-only hypothesis is rejected at 5σ significance. The 5σ-discovery mass reach for the $\eta \to HH$ resonance for different fractional widths and integrated luminosities is shown in Table I.

TABLE I. 5σ discovery mass reach for the $\eta \to HH \to 4\tau$ resonance, at a pp collider with $\sqrt{s} = 100$ TeV, as a function of integrated luminosity $\mathcal{L}$.

$\mathcal{L}$		m_η (TeV)	
(ab^{-1})	$\Gamma/M = 5\%$	$\Gamma/M = 20\%$	$\Gamma/M = 70\%$
1	0.85[a]	1.75	2.81
3	1.33	2.25	3.42
10	1.78	2.90	4.18
30	2.30	3.56	4.94
100	2.90	4.33	5.83

[a] The minimum p_T cuts on the τ lepton have been reduced for this mass point.

Table II shows the dependence of the 5σ-discovery mass reach on the minimum p_T cut applied on the forward tagging jets. The mass reach reduces by about 22% for every 20 GeV increase in the p_T(jet) cut. Thus it is beneficial to maintain as low a p_T(jet) cut as possible. Similarly, the forward rapidity coverage of jets is important. The dependence of the resonance mass reach as a function of the maximum jet rapidity detectable is shown in Table III. Coverage up to jet rapidity of 6-7 is desirable for a 100 TeV pp collider.

TABLE II. 5σ discovery mass reach for the $\eta \to HH \to 4\tau$ resonance, at a pp collider with $\sqrt{s} = 100$ TeV and $\mathcal{L} = 10$ ab^{-1}, for various cuts values on minimum p_T of the forward jets. The fractional width of the η resonance is set to $\Gamma/M = 20\%$.

$p_T^{\min}$ (GeV)	30	50	70	90	110
m_η (TeV)	3.53	2.90	2.35	1.92	1.56

TABLE III. 5σ discovery mass reach for the $\eta \to HH \to 4\tau$ resonance, at a pp collider with $\sqrt{s} = 100$ TeV and $\mathcal{L} = 10$ ab^{-1}, for various cuts values on the maximum rapidity (y) of the forward jets. The fractional width of the η resonance is set to $\Gamma/M = 20\%$.

$y^{\max}$	8	7	6	5	4
m_η (TeV)	2.9	2.9	2.81	2.42	1.75

Tables IV and V summarize the discovery mass reach ($m_\eta^{5\sigma}$) as a function of integrated luminosity ($\mathcal{L}$) and collider center-of-mass energy $\sqrt{s}$, for resonance widths of 20% and 70% respectively. The corresponding results are also presented in Figs. 13 and 14. The figures show that over a wide range of $\mathcal{L}$ and $\sqrt{s}$, $m_\eta^{5\sigma}$ can be described fairly well by a power-law dependence on $\mathcal{L}$,

$$m_\eta^{5\sigma} \propto \mathcal{L}^\alpha \tag{3}$$

where the α values are independent of $\sqrt{s}$. We find that the results of tables IV and V can be parameterized by $\alpha = 0.20$ (0.16) for a resonance width of 20% (70%). Equivalently, an increase in $\mathcal{L}$ by a factor of 10 raises the discoverable mass by 58% (45%). The gain in mass reach with $\mathcal{L}$ is slightly more rapid at low $\mathcal{L}$ and slightly slower at high $\mathcal{L}$.

TABLE IV. 5σ discovery mass reach for the $\eta \to HH \to 4\tau$ resonance, as a function of the $\sqrt{s}$ of a pp collider. The fractional resonance width Γ_η/m_η is fixed at 20%. These results are illustrated in Fig. 13.

$\mathcal{L}$		m_η (TeV)	
(ab^{-1})	$\sqrt{s} = 50$ TeV	$\sqrt{s} = 100$ TeV	$\sqrt{s} = 200$ TeV
1	1.26	1.75	2.27
3	1.58	2.25	2.88
10	2.02	2.90	3.66
30	2.49	3.56	4.44
100	3.06	4.33	5.38

TABLE V. 5σ discovery mass reach for the $\eta \to HH \to 4\tau$ resonance, as a function of the $\sqrt{s}$ of a pp collider. The fractional resonance width Γ_η/m_η is fixed at 70%. These results are illustrated in Fig. 14.

$\mathcal{L}$		m_η (TeV)	
(ab^{-1})	$\sqrt{s} = 50$ TeV	$\sqrt{s} = 100$ TeV	$\sqrt{s} = 200$ TeV
1	1.89	2.81	3.85
3	2.31	3.42	4.65
10	2.83	4.18	5.63
30	3.36	4.94	6.60
100	3.97	5.83	7.74

We also attempt to describe the dependence of $m_\eta^{5\sigma}$ on $\sqrt{s}$ by a power law,

$$m_\eta^{5\sigma} \propto (\sqrt{s})^\beta \tag{4}$$

and find that β values are fairly independent of the integrated luminosity. If $\sqrt{s}$ is increased from 50 TeV to 100 TeV, $\beta = 0.50$ (0.56) for a fractional resonance width of 20% (70%). If $\sqrt{s}$ is increased from 100 TeV to 200 TeV, the corresponding value of the power $\beta = 0.34$ (0.43) fits the results. Thus, the scaling behavior for the discovery mass reach as a function of $\sqrt{s}$ can be approximated by a power-law behavior but the sensitivity gain starts to saturate at the higher collider energies. A reasonable approximation is obtained by fitting the gain from 50 TeV to 200 TeV, yielding $\beta = 0.42$ (0.50) for Γ/M =20% (70%). Equivalently, a doubling of the collider energy increases the discovery mass reach by 33-40% depending on the resonance width, with a somewhat larger (smaller) increase at lower (higher) energies.

It is interesting to evaluate the trade-off between collider energy and integrated luminosity for a given discovery mass reach. For a fractional resonance width of 20% (70%), a factor of two in collider energy is equivalent to a factor of 4.3 (8.7) in integrated luminosity. For a narrow (implying weakly coupled) resonance, integrated luminosity is more effective while for a wide (implying strongly coupled) resonance, collider energy is more effective as a means of increasing the mass reach.

Studies of the sensitivity of the HL-LHC for resonances in vector boson scattering indicate a discovery potential of $m_{\rm res}/g_{\rm res}$ of ≈ 500 GeV [75], where $g_{\rm res}$ is the resonance coupling. While the resonance model and decay channel used in that study were different from ours, the sensitivity from Table I is about a factor of 4-7 higher than that at the LHC. Comparative studies between the HL-LHC and a 100 TeV pp collider [76] regarding the sensitivity to dimension-8 operators in vector boson scattering can also be interpreted as a factor of four higher mass scale being probed at the 100 TeV collider.

VI. CONCLUSIONS

The sensitivity to a resonance in longitudinal VBS in the mass range of 1.5-5 TeV decaying to $HH \to 4\tau$ is discussed for a 100 TeV pp collider. In a benchmark model motivated by the spontaneous breaking of a global $SO(5)$ symmetry to $SO(4)$, the $SU(2)_L$ Higgs doublet field contains the set of four Goldstone modes, which are derivatively coupled to this resonance. The resonance decays democratically to longitudinal $W^{\pm}$ and Z bosons and Higgs bosons with 2:1:1 proportion for the respective branching ratios. We have used leading-order cross sections for the signal and background processes, as the dominant background of VV production ($V = Z, \gamma^*$) in the VBS topology is also purely electroweak and higher-order QCD corrections can be expected to increase the signal and background cross section in comparable proportion.

A reconstruction efficiency for τ leptons of 60% and a corresponding QCD jet efficiency of a few percent is assumed in this study. Future detectors are expected to maintain this τ reconstruction performance, currently achieved by the LHC experiments, at higher transverse momenta with acceptance up to a pseudo-rapidity of 3.

This study shows that, for an integrated luminosity of 10 ab^{-1} at a pp collider with $\sqrt{s} = 100$ TeV, a 5σ discovery reach of 2.90 TeV for the mass of the resonance can be achieved, assuming a width of 20%. For widths varying between 5% and 70%, the corresponding mass reach varies from 1.78 TeV and 4.18 TeV. For a factor of three increase in integrated luminosity, the mass reach increases by 25% (19%) for fractional resonance width of 20% (70%), and this power-law scaling behavior is independent of the collider energy. An approximate power-law scaling dependence on $\sqrt{s}$ is also found, where a doubling of the collider energy increases the discovery mass reach by 33-40% depending on the resonance width, with a larger proportionate increase at lower energies.

The trade-off between collider energy and integrated luminosity for a given discovery mass reach favors luminosity for a narrow, weakly-coupled resonance and energy for a wide, strongly-coupled resonance. For a fractional resonance width of 20% (70%), a factor of two in collider energy is equivalent to a factor of 4.3 (8.7) in integrated luminosity.

New physics in longitudinal vector boson scattering puts strong requirements on the detection of forward jets at high rapidities and low p_T. The mass reach is reduced by about 22% for every 20 GeV increase in the minimum p_T(jet) requirement on the forward tagging jets. A minimum rapidity coverage for the forward jets of 6-7 is desirable. For $p_T(\text{jet}) > 50$ GeV, the mass reach is reduced by 14% if the rapidity coverage is reduced from 6 to 5. Further reducing the rapidity coverage to 4 causes the mass reach to drop by another 28% relative to the coverage of 5. If VBS jets could be distinguished from pileup jets at lower p_T, the gains from extended rapidity coverage would be even higher.

This paper also highlights the importance of the $H \to \tau\tau$ decay channel as a relatively clean mode of identification for double-Higgs production. Distinguishing highly-boosted τ leptons with $p_T(\tau) \sim 1$ TeV from QCD jets and electrons presents a challenge that could be addressed by high-granularity electromagnetic calorimeters. Used in conjunction with tracking detectors having good two-track resolution, such calorimeters could measure the individual charged particles and photons within the τ-jets with sufficient spatial and energy resolution. Resolving the substructure in τ-jets and possibly extracting information on τ polarization could allow future detectors to maintain or even surpass the τ identification efficiency and background rejection that has been demonstrated by the LHC experiments at lower transverse momenta. Thus, the $H \to \tau\tau$ mode could provide a discovery channel for resonant double-Higgs production with good signal-to-background ratio, albeit with low statistics, similar to the $H \to ZZ \to 4\ell$ ($\ell = e, \mu$) channel for the Higgs boson discovery at the LHC. The fact that the $H \to \tau\tau$ branching ratio is approximately equal to the combined branching rato for $Z \to ee, \mu\mu$ supports our emphasis on τ detection.

ACKNOWLEDGMENTS

We thank Kaustubh Agashe, Nima Arkani-Hamed, Roberto Contino, Estia Eichten, Elisabetta Furlan, Zhen Liu, Michelangelo Mangano, Giuliano Panico, Chris Quigg, Raman Sundrum, Liantao Wang, Andrea Wulzer, and Felix Yu for helpful discussions. We thank Benjamin Cerio for his help with the BDT software. The research of S. C. was supported by the Department of Energy Contract No. DE-AC02-06CH11357 at Argonne National Laboratory. The work of A. K. was supported by the Fermi National Accelerator Laboratory and by a Department of Energy grant to Duke University. Fermilab is operated by Fermi Research Alliance, LLC, under Contract No. DE-AC02-07CH11359 with the United States Department of Energy.

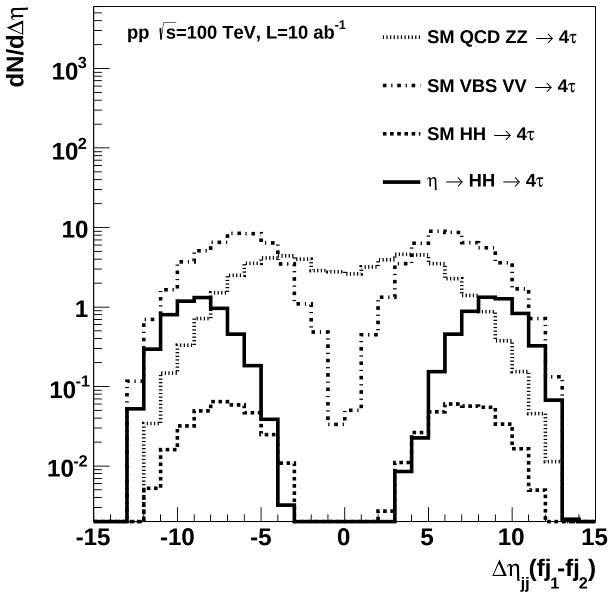

(a)The distribution of the difference $\Delta\eta_{jj}$ in pseudo-rapidities of the two forward jets.

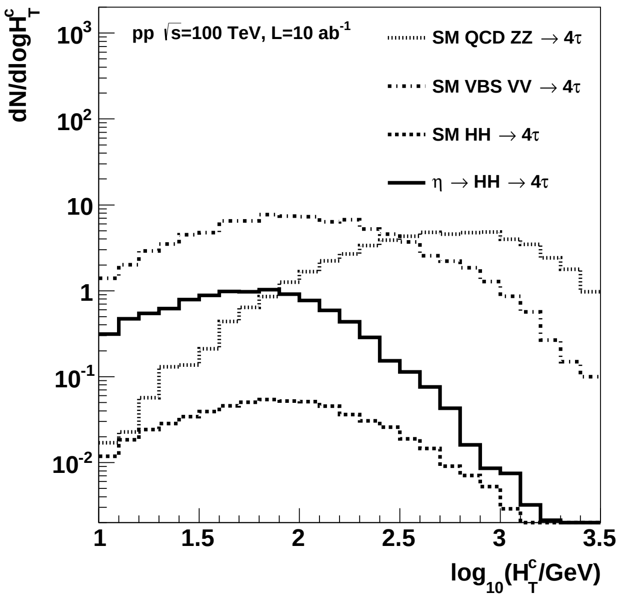

(b)The distribution of H_T^c, the scalar sum of the p_T of the central jets.

FIG. 5. The samples shown in this figure include the generator-level cuts $m_{jj} > 1.5$ TeV, and p_T(jet) > 50 GeV. The distributions motivate the additional requirements of $|\Delta\eta_{jj}| > 5$ and $H_T^c < 300$ GeV.

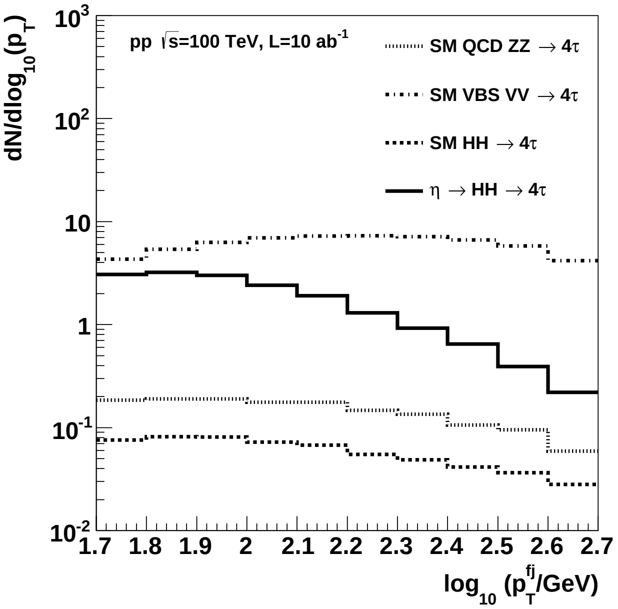

(a)The p_T distribution of forward jets.

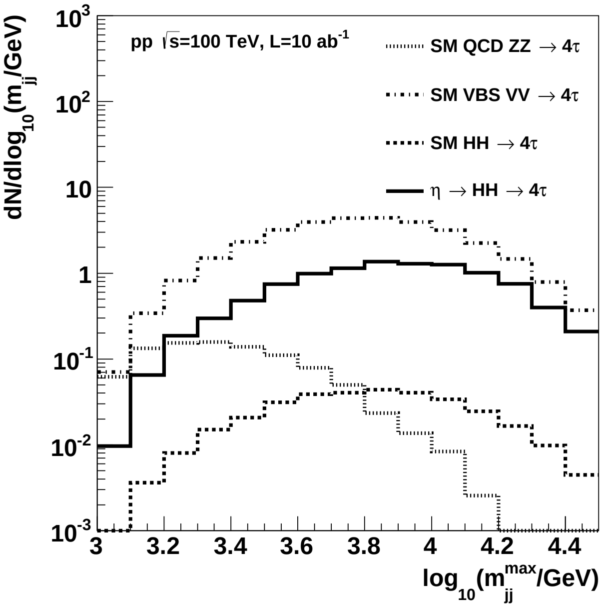

(b)The distribution of dijet mass of the forward jets.

FIG. 6. The p_T and dijet mass distributions of the two forward jets. The samples shown in this figure and subsequent figures include the generator-level cuts $m_{jj} > 1.5$ TeV, $50 < p_T$(jet) < 500 GeV, $|\eta$(jet)$| > 2$, $|\Delta\eta_{jj}| > 5$ and $H_T^c < 300$ GeV.

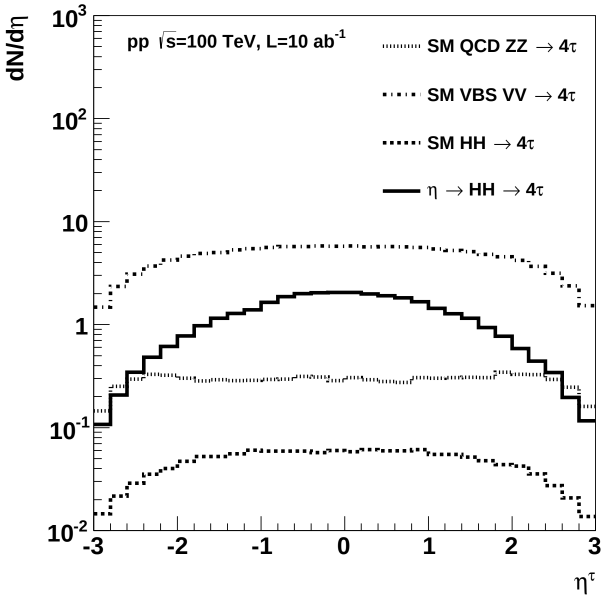

(a)The pseudo-rapidity distribution of τ-jets.

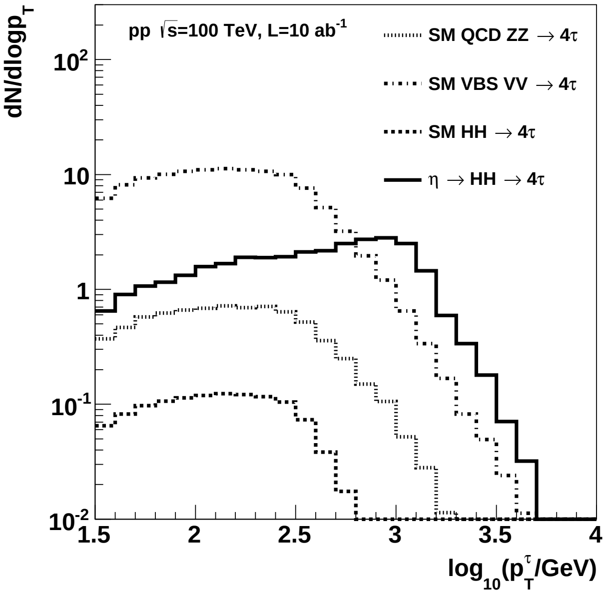

(b)The p_T distribution of τ-jets.

FIG. 7. The pseudo-rapidity and p_T distributions of τ-jets.

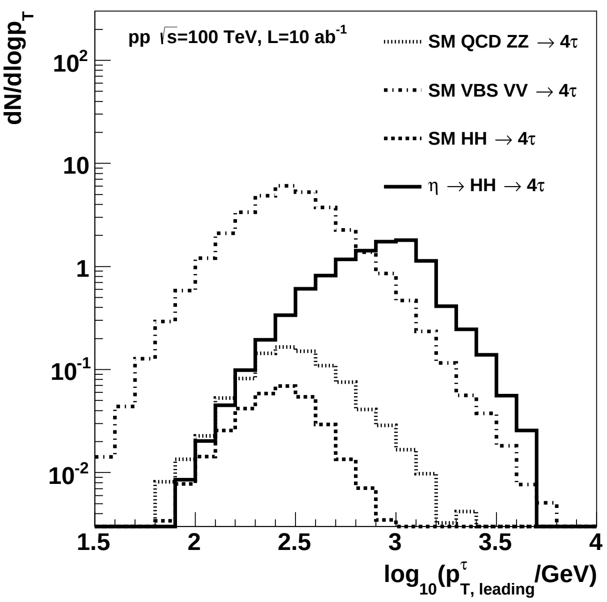

(a)The p_T distribution of the leading τ-jet.

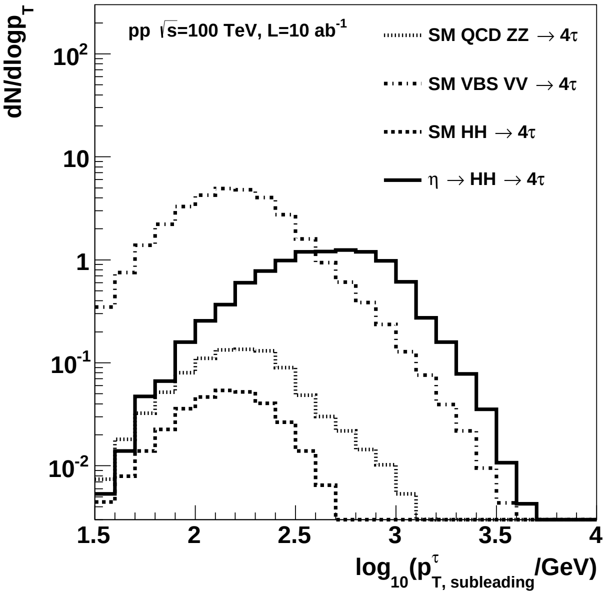

(b)The p_T distribution of the next-to-leading τ-jet.

FIG. 8. The p_T distributions of the highest-p_T τ-jets.

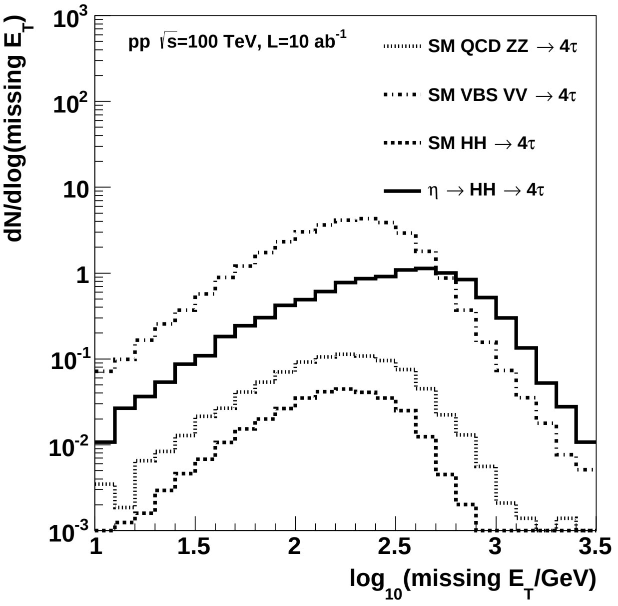

FIG. 9. The distributions of $\not{E}_{\mathrm{T}}$.

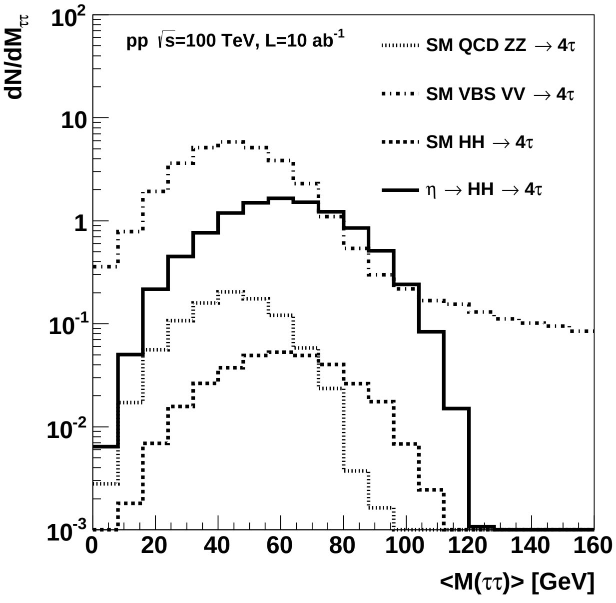

FIG. 10. The distribution of the per-event average of the reconstructed masses of the τ-jet pairs from $V \to \tau\tau$ ($H \to \tau\tau$) in $VVjj$ ($HHjj$) events, where $V = \gamma^*/Z$.

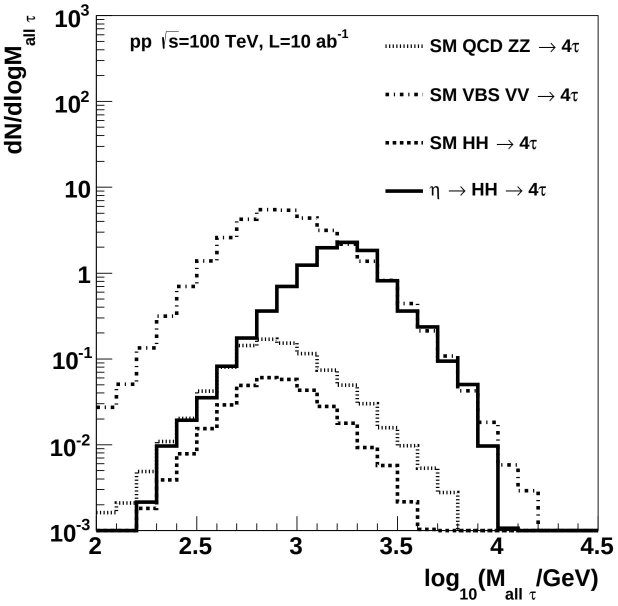

(a)The distribution of invariant mass of all reconstructed τ-jets.

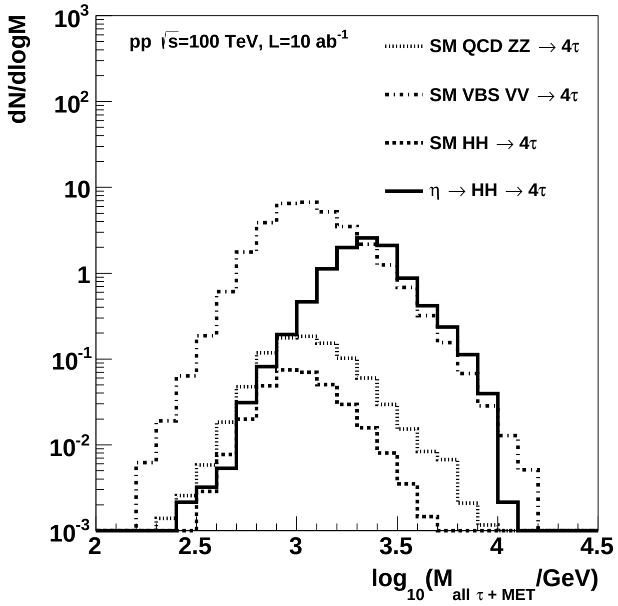

(b)The distribution of invariant mass of all reconstructed τ-jets and $\not{E}_{\mathrm{T}}$, setting $\not{E}_z = 0$.

FIG. 11. The invariant-mass distributions involving multiple reconstructed τ-jets.

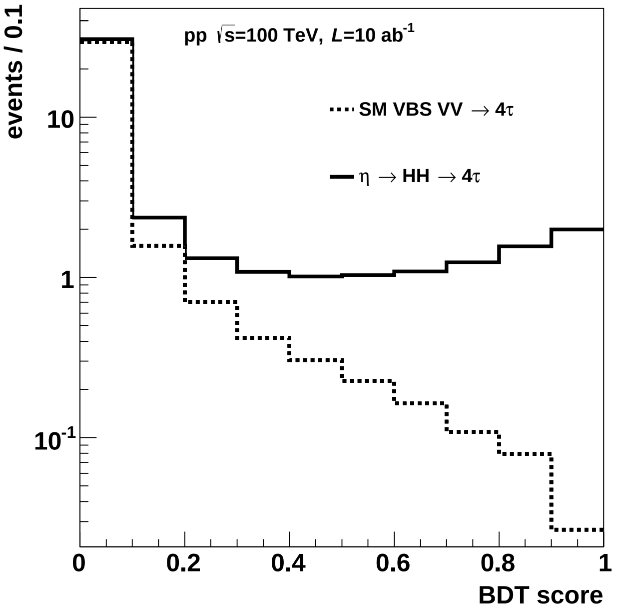

FIG. 12. The distributions of the BDT score for the $\eta \to HH \to 4\tau$ signal with $m_\eta = 3$ TeV, and the VBS $VV \to 4\tau$ background, where $V = \gamma^*/Z$.

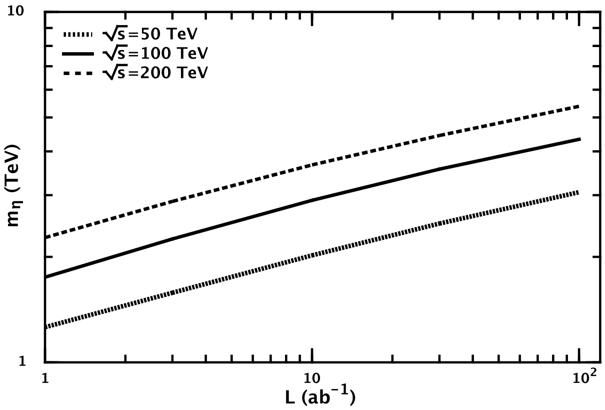

FIG. 13. 5σ discovery mass reach for the $\eta \to HH \to 4\tau$ resonance, as a function of the integrated luminosity and $\sqrt{s}$ of a pp collider. The fractional resonance width Γ_η/m_η is fixed at 20%.

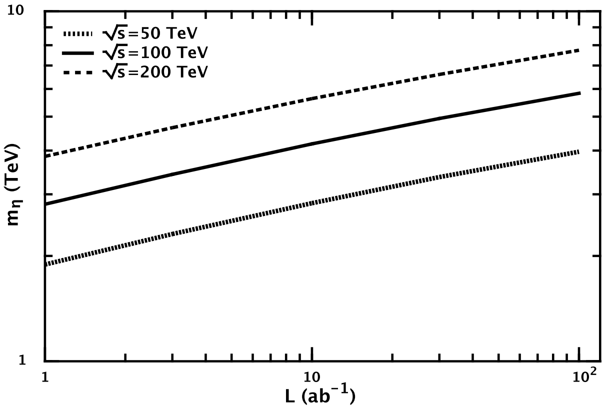

FIG. 14. 5σ discovery mass reach for the $\eta \to HH \to 4\tau$ resonance, as a function of the integrated luminosity and $\sqrt{s}$ of a pp collider. The fractional resonance width Γ_η/m_η is fixed at 70%.

[1] G. Aad *et al.* (ATLAS Collaboration), Phys. Lett. **B716**, 1 (2012), arXiv:1207.7214 [hep-ex].

[2] S. Chatrchyan *et al.* (CMS Collaboration), Phys. Lett. **B716**, 30 (2012), arXiv:1207.7235 [hep-ex].

[3] S. Weinberg, Phys.Rev.Lett. **19**, 1264 (1967).

[4] A. Salam, (1969), proc. of the 8th Nobel Symposium on 'Elementary particle theory, relativistic groups and analyticity', Stockholm, Sweden, 1968, edited by N. Svartholm, p.367-377.

[5] Y. Nambu, Phys.Rev.Lett. **4**, 380 (1960).

[6] J. Goldstone, Nuovo Cim. **19**, 154 (1961).

[7] J. Goldstone, A. Salam, and S. Weinberg, Phys.Rev. **127**, 965 (1962).

[8] F. Englert and R. Brout, Phys.Rev.Lett. **13**, 321 (1964).

[9] P. W. Higgs, Phys.Lett. **12**, 132 (1964).

[10] P. W. Higgs, Phys.Rev.Lett. **13**, 508 (1964).

[11] G. Guralnik, C. Hagen, and T. Kibble, Phys.Rev.Lett. **13**, 585 (1964).

[12] G. 't Hooft, NATO Sci.Ser.B **59**, 135 (1980).

[13] H. Georgi and D. B. Kaplan, Phys.Lett. **B145**, 216 (1984).

[14] H. Georgi, D. B. Kaplan, and P. Galison, Phys.Lett. **B143**, 152 (1984).

[15] D. B. Kaplan and H. Georgi, Phys.Lett. **B136**, 183 (1984).

[16] M. J. Dugan, H. Georgi, and D. B. Kaplan, Nucl.Phys. **B254**, 299 (1985).

[17] K. Agashe, R. Contino, and A. Pomarol, Nucl.Phys. **B719**, 165 (2005), arXiv:hep-ph/0412089 [hep-ph].

[18] R. Contino, L. Da Rold, and A. Pomarol, Phys.Rev. **D75**, 055014 (2007), arXiv:hep-ph/0612048 [hep-ph].

[19] R. Contino, D. Marzocca, D. Pappadopulo, and R. Rattazzi, JHEP **1110**, 081 (2011), arXiv:1109.1570 [hep-ph].

[20] J. Bagger, V. D. Barger, K.-m. Cheung, J. F. Gunion, T. Han, *et al.*, Phys.Rev. **D49**, 1246 (1994), arXiv:hep-ph/9306256 [hep-ph].

[21] J. Bagger, V. D. Barger, K.-m. Cheung, J. F. Gunion, T. Han, *et al.*, Phys.Rev. **D52**, 3878 (1995), arXiv:hep-ph/9504426 [hep-ph].

[22] M. Cacciari, G. P. Salam, and G. Soyez, JHEP **04**, 063 (2008), arXiv:0802.1189 [hep-ph].

[23] M. Cacciari, G. Salam, and G. Soyez, "FastJet. A C++ library for the k_T algorithm," Http://www.lpthe.jussieu.fr/ salam/fastjet/.

[24] A. Hook and A. Katz, JHEP **1409**, 175 (2014), arXiv:1407.2607 [hep-ph].

[25] M. Cirelli, F. Sala, and M. Taoso, (2014), arXiv:1407.7058 [hep-ph].

[26] J. Bramante, P. J. Fox, A. Martin, B. Ostdiek, T. Plehn, *et al.*, (2014), arXiv:1412.4789 [hep-ph].

[27] D. Curtin, P. Meade, and C.-T. Yu, (2014), arXiv:1409.0005 [hep-ph].

[28] N. Craig, H. K. Lou, M. McCullough, and A. Thalapillil, (2014), arXiv:1412.0258 [hep-ph].

[29] A. Ismail, I. Low, M. Low, and L.-T. Wang, (in preparation).

[30] A. Berlin, T. Lin, M. Low, and L.-T. Wang, (2015), arXiv:1502.05044 [hep-ph].

[31] A. Pierce, J. Thaler, and L.-T. Wang, JHEP **0705**, 070 (2007), arXiv:hep-ph/0609049 [hep-ph].

[32] R. Contino, C. Grojean, M. Moretti, F. Piccinini, and R. Rattazzi, JHEP **1005**, 089 (2010), arXiv:1002.1011 [hep-ph].

[33] R. Contino, M. Ghezzi, M. Moretti, G. Panico, F. Piccinini, *et al.*, JHEP **1208**, 154 (2012), arXiv:1205.5444 [hep-ph].

[34] M. J. Dolan, C. Englert, and M. Spannowsky, JHEP **1210**, 112 (2012), arXiv:1206.5001 [hep-ph].

[35] M. J. Dolan, C. Englert, and M. Spannowsky, Phys.Rev. **D87**, 055002 (2013), arXiv:1210.8166 [hep-ph].

[36] A. J. Barr, M. J. Dolan, C. Englert, and M. Spannowsky, Phys.Lett. **B728**, 308 (2014), arXiv:1309.6318 [hep-ph].

[37] M. J. Dolan, C. Englert, N. Greiner, and M. Spannowsky, Phys.Rev.Lett. **112**, 101802 (2014), arXiv:1310.1084 [hep-ph].

[38] C.-R. Chen and I. Low, Phys.Rev. **D90**, 013018 (2014), arXiv:1405.7040 [hep-ph].

[39] A. J. Barr, M. J. Dolan, C. Englert, D. E. Ferreira de Lima, and M. Spannowsky, JHEP **1502**, 016 (2015), arXiv:1412.7154 [hep-ph].

[40] A. Azatov, R. Contino, G. Panico, and M. Son, (2015), arXiv:1502.00539 [hep-ph].

[41] J. M. No and M. Ramsey-Musolf, Phys.Rev. **D89**, 095031 (2014), arXiv:1310.6035 [hep-ph].

[42] S. Dawson, A. Ismail, and I. Low, (2015), arXiv:1504.05596 [hep-ph].

[43] A. Papaefstathiou, L. L. Yang, and J. Zurita, Phys.Rev. **D87**, 011301 (2013), arXiv:1209.1489 [hep-ph].

[44] P. Maierhöfer and A. Papaefstathiou, JHEP **1403**, 126 (2014), arXiv:1401.0007 [hep-ph].

[45] D. E. Ferreira de Lima, A. Papaefstathiou, and M. Spannowsky, JHEP **1408**, 030 (2014), arXiv:1404.7139 [hep-ph].

[46] F. Goertz, A. Papaefstathiou, L. L. Yang, and J. Zurita, JHEP **1504**, 167 (2015), arXiv:1410.3471 [hep-ph].

[47] A. Papaefstathiou, (2015), arXiv:1504.04621 [hep-ph].

[48] B. Bhattacherjee and A. Choudhury, Phys. Rev. D **91**, 073015 (2015).

[49] Q. Li, Z. Li, Q.-S. Yan, and X. Zhao, (2015), arXiv:1503.07611 [hep-ph].

[50] K. Olive *et al.* (Particle Data Group), Chin.Phys. **C38**, 090001 (2014).

[51] U. Baur, T. Plehn, and D. L. Rainwater, Phys.Rev. **D69**, 053004 (2004), arXiv:hep-ph/0310056 [hep-ph].

[52] F. Goertz, A. Papaefstathiou, L. L. Yang, and J. Zurita, JHEP **1306**, 016 (2013), arXiv:1301.3492 [hep-ph].

[53] V. Barger, L. L. Everett, C. Jackson, and G. Shaughnessy, Phys.Lett. **B728**, 433 (2014), arXiv:1311.2931 [hep-ph].

[54] J. Baglio, A. Djouadi, R. Gröber, M. Mühlleitner, J. Quevillon, *et al.*, JHEP **1304**, 151 (2013), arXiv:1212.5581 [hep-ph].

[55] W. Yao, (2013), arXiv:1308.6302 [hep-ph].

[56] J. de Favereau *et al.* (DELPHES 3), JHEP **1402**, 057 (2014), arXiv:1307.6346 [hep-ex].

[57] J. Anderson, A. Avetisyan, R. Brock, S. Chekanov, T. Cohen, *et al.*, (2013), arXiv:1309.1057 [hep-ex].

[58] T. Sjostrand, S. Mrenna, and P. Z. Skands, JHEP **05**, 026 (2006), arXiv:hep-ph/0603175.

[59] S. Chekanov, "HepSim: a repository with predictions for high-energy physics experiments," (2014),

http://atlaswww.hep.anl.gov/hepsim/, arXiv:1403.1886 [hep-ph].

[60] ATLAS Collaboration, "Identification and energy calibration of hadronically decaying tau leptons with the ATLAS experiment in pp collisions at $\sqrt{s} = 8$ TeV," (2009), arXiv:1412.7086.

[61] ATLAS Collaboration, "A search for high-mass ditau resonances decaying in the fully hadronic final state in pp collisions at $\sqrt{s} = 8$ TeV with the ATLAS detector," (2009), ATLAS-CONF-2013-066.

[62] ATLAS Collaboration, Phys. Lett. **B719**, 242 (2013), arXiv:1210.6604.

[63] ATLAS Collaboration, "Performance of the Reconstruction and Identification of Hadronic Tau Decays with ATLAS," (2011), ATLAS-CONF-2011-152.

[64] ATLAS Collaboration, "Search for resonant diboson production in the $\ell\ell q\bar{q}$ final state in pp collisions at $\sqrt{s} = 8$ TeV with the ATLAS detector," (2015), arXiv:1409.6190.

[65] J. Alwall, M. Herquet, F. Maltoni, O. Mattelaer, and T. Stelzer, JHEP **1106**, 128 (2011), arXiv:1106.0522 [hep-ph].

[66] A. Martin, W. Stirling, R. Thorne, and G. Watt, Eur.Phys.J. **C63**, 189 (2009), arXiv:0901.0002 [hep-ph].

[67] S. V. Chekanov, "Next generation input-output data format for HEP using Google's protocol buffers," (2013), arXiv:1306.6675 [cs.CE].

[68] S. Chekanov, E. May, K. Strand, and P. V. Gemmeren, Computer Physics Communications **185**, 2629 (2014), arXiv:1311.1229 [physics.comp-ph].

[69] I. Antcheva *et al.*, Comput. Phys. Commun. **180**, 2499 (2009).

[70] ATLAS Collaboration, "Studies of Vector Boson Scattering And Triboson Production with an Upgraded ATLAS Detector at a High-Luminosity LHC," (2013), ATL-PHYS-PUB-2013-006.

[71] CMS Collaboration, "Vector Boson Scattering and Quartic Gauge Coupling Studies in WZ Production at 14 TeV," (2013), CMS-PAS-FTR-13-006.

[72] G. Aad *et al.* (ATLAS Collaboration), Phys. Rev. Lett. **113**, 141803 (2014).

[73] J. Baglio *et al.*, (2014), arXiv:1107.4038 [hep-ph].

[74] M.-A. Pleier, Private communication. We thanks Marc-Andre Pleier for computing the NLO QCD k-factor for diboson processes using the VBFNLO v2.7.0 program.

[75] ATLAS Collaboration, "Studies of Vector Boson Scattering with an Upgraded ATLAS Detector at a High-Luminosity LHC," (2012), ATLAS-PHYS-PUB-2012-005.

[76] M. Baak *et al.*, (2013), arXiv:1310.6708 [hep-ph].

APPENDIX

Decay channel	Branching ratio	Uncertainty
$b\bar{b}b\bar{b}$	$3.33 \cdot 10^{-1}$	$\pm 2.20 \cdot 10^{-2}$
$\tau\tau b\bar{b}$	$7.29 \cdot 10^{-2}$	$\pm 4.80 \cdot 10^{-3}$
$W^+(\to l\nu)W^-(\to l\nu)b\bar{b}$	$1.09 \cdot 10^{-2}$	$\pm 5.93 \cdot 10^{-4}$
$\tau\tau\tau\tau$	$3.99 \cdot 10^{-3}$	$\pm 4.55 \cdot 10^{-4}$
$\gamma\gamma b\bar{b}$	$2.63 \cdot 10^{-3}$	$\pm 1.58 \cdot 10^{-4}$
$W^+(\to l\nu)W^-(\to l\nu)\tau\tau$	$1.20 \cdot 10^{-3}$	$\pm 8.56 \cdot 10^{-5}$
$\gamma\gamma\tau\tau$	$2.88 \cdot 10^{-4}$	$\pm 2.19 \cdot 10^{-5}$
$b\bar{b}\mu^+\mu^-$	$2.53 \cdot 10^{-4}$	$\pm 1.73 \cdot 10^{-5}$
$Z(\to l^+l^-)Z(\to l^+l^-)b\bar{b}$	$1.41 \cdot 10^{-4}$	$\pm 7.64 \cdot 10^{-6}$
$b\bar{b}Z(\to l^+l^-)\gamma$	$1.21 \cdot 10^{-4}$	$\pm 1.16 \cdot 10^{-5}$
$W^+(\to l\nu)W^-(\to l\nu)W^+(\to l\nu)W^-(\to l\nu)$	$8.99 \cdot 10^{-5}$	$\pm 7.73 \cdot 10^{-6}$
$\gamma\gamma W^+(\to l\nu)W^-(\to l\nu)$	$4.32 \cdot 10^{-5}$	$\pm 2.85 \cdot 10^{-6}$
$\tau\tau\mu^+\mu^-$	$2.77 \cdot 10^{-5}$	$\pm 2.29 \cdot 10^{-6}$
$Z(\to l^+l^-)Z(\to l^+l^-)\tau\tau$	$1.54 \cdot 10^{-5}$	$\pm 1.10 \cdot 10^{-6}$
$\tau\tau Z(\to l^+l^-)\gamma$	$1.32 \cdot 10^{-5}$	$\pm 1.41 \cdot 10^{-6}$
$\gamma\gamma\gamma\gamma$	$5.20 \cdot 10^{-6}$	$\pm 5.20 \cdot 10^{-7}$
$W^+(\to l\nu)W^-(\to l\nu)\mu^+\mu^-$	$4.15 \cdot 10^{-6}$	$\pm 3.07 \cdot 10^{-7}$
$Z(\to l^+l^-)Z(\to l^+l^-)W^+(\to l\nu)W^-(\to l\nu)$	$2.31 \cdot 10^{-6}$	$\pm 1.41 \cdot 10^{-7}$
$W^+(\to l\nu)W^-(\to l\nu)Z(\to l^+l^-)\gamma$	$1.99 \cdot 10^{-6}$	$\pm 1.98 \cdot 10^{-7}$
$\gamma\gamma\mu^+\mu^-$	$9.99 \cdot 10^{-7}$	$\pm 7.80 \cdot 10^{-8}$
$\gamma\gamma Z(\to l^+l^-)Z(\to l^+l^-)$	$5.57 \cdot 10^{-7}$	$\pm 3.67 \cdot 10^{-8}$
$\gamma\gamma Z(\to l^+l^-)\gamma$	$4.78 \cdot 10^{-7}$	$\pm 4.92 \cdot 10^{-8}$
$Z(\to l^+l^-)Z(\to l^+l^-)\mu^+\mu^-$	$5.35 \cdot 10^{-8}$	$\pm 3.95 \cdot 10^{-9}$
$Z(\to l^+l^-)\gamma\mu^+\mu^-$	$4.59 \cdot 10^{-8}$	$\pm 4.96 \cdot 10^{-9}$
$Z(\to l^+l^-)Z(\to l^+l^-)Z(\to l^+l^-)\gamma$	$2.56 \cdot 10^{-8}$	$\pm 2.55 \cdot 10^{-9}$
$Z(\to l^+l^-)Z(\to l^+l^-)Z(\to l^+l^-)Z(\to l^+l^-)$	$1.49 \cdot 10^{-8}$	$\pm 1.28 \cdot 10^{-9}$
$Z(\to l^+l^-)\gamma Z(\to l^+l^-)\gamma$	$1.10 \cdot 10^{-8}$	$\pm 1.97 \cdot 10^{-9}$

TABLE VI. Branching ratios for final states arising from double-Higgs production, with the requirement of leptonic decays of W and Z bosons.

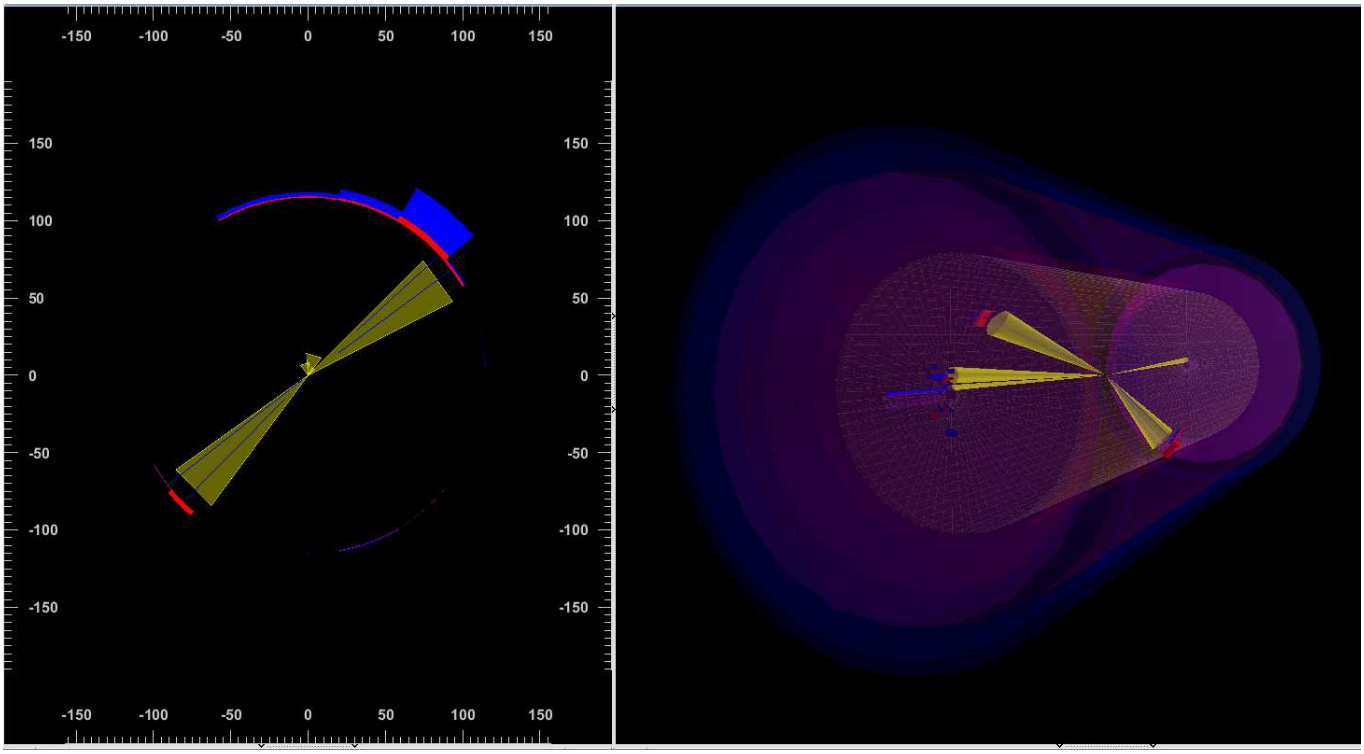

FIG. 15. An event display showing the η resonance ($m_\eta = 3$ TeV) produced via longitudinal vector boson scattering, and decaying to $HH \to 4\tau$ at a 100 TeV pp collider. (left) In the transverse view, two forward jets with transverse momenta above 50 GeV are shown with the small yellow cones, and two jets arising from $H \to \tau\tau$ are shown with the large yellow cones. (right) A 3D view of the same event. The jets are reconstructed using the anti-k_T algorithm [22] using the FastJet package [23]. The event display was created using the Delphes fast simulation [56], HepSim [59] and the Snowmass detector setup [57]. The blue lines show charged hadrons. See the text for details.